Ambipolar charge transport in a non-fullerene acceptor

Cite as: APL Mater. 11, 021105 (2023); doi: 10.1063/5.0137073
Submitted: 30 November 2022 • Accepted: 23 January 2023 •
Published Online: 13 February 2023

Franziska H. Hasenburg, Kun-Han Lin, Bas van der Zee, Paul W. M. Blom, Denis Andrienko, and Gert-Jan A. H. Wetzelaer[a)]

AFFILIATIONS

Max Planck Institute for Polymer Research, Ackermannweg 10, 55128 Mainz, Germany

Note: This paper is part of the Special Topic on Advances in Organic Solar Cells.
[a)]**Author to whom correspondence should be addressed:** wetzelaer@mpip-mainz.mpg.de

ABSTRACT

Charge transport is one of the key factors in the operation of organic solar cells. Here, we investigate the electron and hole transport in the non-fullerene acceptor (NFA) IT-4F, by a combination of space-charge-limited current measurements and multiscale molecular simulations. The electron and hole mobilities are fairly balanced, amounting to 2.9×10^{-4} cm^2 V^{-1} s^{-1} for electrons and 2.0×10^{-5} cm^2 V^{-1} s^{-1} for holes. Orientational ordering and electronic couplings facilitate a better charge-percolating network for electrons than for holes, while ambipolarity itself is due to sufficiently high electron affinity and low ionization energy typical for narrow-gap NFAs. Our findings provide a molecular-level understanding of the balanced hole and electron transport in an archetypical NFA, which may play a key role in exciton diffusion and photogenerated hole transfer in organic solar cells.

INTRODUCTION

Non-fullerene acceptor (NFA) materials revolutionized the field of organic photovoltaics, making their commercialization tangible.[1–4] Most successful of them are fused-ring electron acceptors with an electron-pushing backbone and electron-pulling end-capping units.[5,6] Solar cells with NFAs based on this molecular design[7] have power-conversion efficiencies (PCEs) of up to 20%.[6,8–11] Despite the progress in the PCE, only limited research has been performed on charge transport in NFAs. Charge transport directly impacts the performance of solar cells,[12] while the electron and hole transport may also be relevant to exciton diffusion.[13] The electron transport in several NFAs has so far been characterized by means of space-charge-limited current (SCLC), time-of-flight (TOF), and field-effect transistor (FET) measurements.[14–18] A general issue with TOF measurements is that the transients are often dispersive, giving rise to a time-dependent mobility. Indeed, a recent study on the electron transport in two NFAs[15] shows a highly dispersive transport, possibly due to energetic disorder. Such dispersive transport may not necessarily reflect the (time-averaged) steady-state transport relevant to solar cells.[19]

Field-effect transistor measurements may also not reflect the bulk transport relevant to solar cells, as in an FET, the transport in a horizontal plane adjacent to the gate dielectric is probed. In addition, charge-carrier densities are substantially higher in FETs, compared to solar cells.[20] SCLC measurements, on the other hand, are ideally suited to probe the steady-state transport in the bulk. However, the SCLC measurements of NFAs published to date provide little detail on the charge-transport characteristics.[16,21] In addition, for SCLC measurements to be reliable, they have to be performed on devices without charge-injection barriers at the contacts, which is difficult to achieve.

Apart from the electron transport, little is known about the hole transport in NFAs. Organic semiconductors are generally capable of transporting both electrons and holes, depending on their energy levels with respect to an energetic window in which charge transport is trap-free.[22] Efficient NFAs seem to have energy levels within or close to this energetic window. While the benefit of trap-free *electron* transport is obvious for solar cells, efficient hole transport might be key for long-range exciton diffusion, which is one of the reasons for the efficient operation of NFA-based solar cells.

In a recent study, it was found that the non-fullerene acceptor IT-4F has an exciton diffusion length of up to 45 nm, the longest among a series of NFAs.[13] In addition, FET measurements demonstrate ambipolar characteristics.[13] IT-4F has been among the best-performing acceptors in the first generation of NFAs,[16] guiding the development of recent NFAs.[23,24] In a binary blend with the donor polymer PM6, a record-breaking PCE value of 13.5% was reported,[25] while IT-4F scores among the compounds with the highest spectrally averaged internal quantum efficiency values.[26] The good performance of IT-4F in terms of internal quantum efficiency, exciton diffusion length, and its molecular structure as a predecessor for high-performance NFAs makes it an ideal model compound for a detailed study on its charge-transport characteristics.

Here, we investigate the electron and hole transport in pristine films of the non-fullerene acceptor IT-4F. Temperature-dependent space-charge-limited current measurements are analyzed with drift-diffusion simulations, revealing that the electron and hole transport is fairly balanced, differing by about an order of magnitude. These experimental observations are corroborated by computer simulations, which further reveal that the balanced charge transport is a result of molecular ordering.

METHODS

Device fabrication

IT-4F was purchased from Ossila Ltd. and used as received. All other materials were purchased from Sigma-Aldrich.

The device fabrication and characterization were performed under nitrogen atmosphere (O_2 < 0.1 ppm; H_2O < 0.1 ppm). Electron-only devices were fabricated in a glass/Al(30 nm)/IT-4F(200 nm)/TPBi(4 nm)/Ba(5 nm)/Al(100 nm) structure, where the interlayer of TPBi (1,3,5-tris(N-phenylbenzimidazol-2-yl)benzene) enables injection via electron tunneling,[27] enhancing the current density by 1.5 orders of magnitude at an applied bias of 4 V. The layer stack of the hole-only devices is glass/Au(30 nm)/PEDOT:PSS(40 nm)/IT-4F(200 nm)/MoO_3(10 nm)/Al(100 nm), where PEDOT:PSS denotes poly(3,4-ethylenedioxythiophene)–poly(styrenesulfonate). Introducing an additional fullerene (C60) tunneling interlayer[27] between IT-4F and MoO_3 did not improve the hole injection, indicating that the MoO_3 contact is already Ohmic. The device area amounted to 1 mm^2 for all devices. A small device area was used to keep the current through the device low, ensuring a negligible voltage drop due to the series resistance of the electrodes in the measured current range.

The metals and metal oxides were evaporated at a base pressure of around 3×10^{-7} mbar and TPBi was evaporated at around 2×10^{-6} mbar, whereas PEDOT:PSS and IT-4F were solution processed. PEDOT:PSS was deposited using spin coating, and the layer was subsequently annealed for 10 min at 140 °C. IT-4F was spin coated from a chlorobenzene solution (23 mg/ml, stirred overnight at 60 °C) at a speed of 1000 rpm for 70 s. Annealing for 10 min at 140 °C had no influence on the electrical properties. PM6 was spin coated from chlorobenzene solution (15 mg/ml, stirred overnight at 60 °C) at a speed of 2000 rpm for 60 s. Layer thicknesses were measured with a DektakXT® stylus profilometer.

Electrical characterization was performed with a Keithley 2400 source meter. The devices were not exposed to ambient air until after device characterization.

Drift-diffusion modeling

To characterize the charge transport, numerical 1D drift-diffusion simulations[28] were fitted to the experimentally obtained, temperature-dependent J–V characteristics. Temperature-, field-, and density-dependent mobilities in the framework of the extended Gaussian disorder model (EGDM) were used to describe the experimental data (see the supplementary material for further information on the drift-diffusion solver).[29]

The fitting procedure first involves estimating the charge-carrier mobility parameters, whereas trapping parameters are included in the second step. The mobility can be fitted in the high-voltage regime, where all traps are filled. In the EGDM, there are three fit parameters: a mobility prefactor μ_∞, the width of the DOS distribution σ, and the lattice constant a. Here, σ mainly controls the temperature dependence, whereas a predominantly affects the field dependence and μ_∞ controls the magnitude of the mobility. Trapping is added subsequently by using a Gaussian distribution of trap states. The trap density influences the voltage at which trap filling is completed, i.e., the trap-filled limit, whereas the trap depth influences the magnitude of the current below the trap-filled limit.[30]

Multiscale molecular simulations

Force field parameterization

All bonded parameters were taken from the empirical OPLS-AA force field[31,32] and our previous work.[33] The non-bonded parameters, atomic partial charges, and Lennard-Jones parameters were derived following the protocol proposed by Cole *et al.*[34] In short, the overlapping atomic electron densities were obtained via the density-derived electrostatic and chemical (DDEC6) electron density partitioning scheme.[35] On the one hand, the atomic partial charges can then be obtained by integrating the corresponding atomic electron densities over the whole space. On the other hand, the two parameters, A and B, in the Lennard-Jones potential were derived using the Tkatchenko–Scheffler (TS) scheme[36] and the radius of the free atom in a vacuum was taken from Ref. 34. The electron density was obtained by using Gaussian16[37] at ωB97X-D/6-311G(d,p) level, and the DDEC6 computations were performed using Chargemol of version 09_26_2017.[38] All molecules considered in this work were partitioned into several rigid fragments following the same procedure as our previous work.[33] After non-bonded parameters were set, the dihedral potentials that connect these rigid fragments were parameterized using the constrained optimization scanning performed at ωB97X-D/6-311G(d,p) level using Gaussian16. For more details on the parameterization of dihedral potentials, please refer to Ref. 38.

Simulated amorphous morphology

To construct the amorphous morphology, 2000 IT-4F molecules were initially randomly placed in a simulation box with a low target density of around 100 kg/m^3 using Packmol.[39]

The whole system was then compressed and heated up to 800 K with an NPT barostat followed by a 10 ns equilibration at 800 K. Finally, the system underwent a linear cooling procedure from 800 to 300 K at a 500 K/ns cooling rate, followed by a further equilibration at 300 K for 9 ns. The second-rank orientational order parameter[40] $\overline{P}_2$ of the final snapshot of the trajectory is calculated to be 0.04.

As for the smectic phase, 2000 IT-4F molecules were placed on the simple cubic lattice sites without relative rotation. The whole system was then compressed and heated up to 500 K with an NPT barostat, followed by a 10 ns equilibration at 500 K. Finally, the system underwent a linear cooling procedure from 500 to 300 K at a 500 K/ns cooling rate followed by a further equilibration at 300 K for 9 ns. The $\overline{P}_2$ of the final snapshot of the trajectory is calculated to be 0.65.

For the crystalline phase, we created a supercell with 2000 molecules from an experimental crystal structure.[7] The whole system was then equilibrated at 300 K for 10 ns. The $\overline{P}_2$ of the final snapshot of the trajectory is calculated to be around 1.0.

All classical MD simulations were performed using GROMACS version 2020.3.[41,42] For the long-range electrostatic interactions, the particle mesh Ewald (PME) method was employed with a 0.12 nm Fourier spacing. A cutoff of 13 Å was applied to all non-bonded interactions. The temperature and pressure control was accomplished using velocity rescaling with a stochastic term (τ_T = 0.5 ps) and an isotropic coupling for the pressure from a Berendsen barostat (P_0 = 1 bar, χ = 4.5 × 10^{-5} bar^{-1}, and τ_P = 0.5 ps).

Site energy computation

The ionization energy (*IE*) and electron affinity (*EA*) in the bulk were computed using a perturbative way, with the solid-state charge stabilization computed using atomic multipoles and the Thole model.[43]

For the gas-phase computations, the geometry of the neutral IT-4F was optimized using the ωB97X-D* functional and 6-311G(d,p) basis set. The optimal ω was obtained following the same ω-tuning procedure we used in our previous work.[33] The electronic total energy of cationic and anionic IT-4F was evaluated using the neutral optimized geometry and the same level of theory. This is used to calculate the gas-phase *IE* and *EA* shown in Fig. 2; $IE_{gas} = E_{nN} - E_{cN}$ and $EA_{gas} = E_{aN} - E_{nN}$, where E_{nN}, E_{aN}, and E_{cN} are the electronic total energy of neutral, anionic, and cationic IT-4F molecules evaluated at the optimized neutral geometry.

The atomic multipoles for all states (n, c, a) and geometries (N, C, A) were derived using the DDEC6 method. The atomic polarizabilities of all states were obtained by linearly scaling the isotropic atomic polarizabilities of the AMOEBA force field. The scaling factor is the value at which the effective molecular polarizable volumes of the QM computations and this method match. These two properties were evaluated using B3LYP/6-311G(d,p). All computations mentioned above were performed using Gaussian16.[37]

The atomic multipoles and polarizabilities were then mapped onto the simulated morphology obtained via MD simulations. The solid-state stabilization for each molecule (site) in the solid was then computed using the long-range embedding approach[44] implemented in VOTCA.[43]

Transfer integrals

The transfer integrals were evaluated for all molecular pairs (dimers) within the 7 Å nearest-atomic-distance cutoff in the molecular solids. We utilize the cost-efficient MOO-ZINDO method[45] to calculate the transfer integrals, which has shown to give reasonable results.[46]

Reorganization energy

The gas-phase reorganization energy is computed using the four-point method,[47] $\lambda_h = (E_{cN} - E_{cC}) + (E_{nC} - E_{nN})$ and $\lambda_e = (E_{aN} - E_{aA}) + (E_{nA} - E_{nN})$, where λ_h and λ_e are the reorganization energy for hole and electron transfers, respectively. E_{nN}, E_{aN}, and E_{cN} follow the same definition as before. E_{aA} and E_{cC} are the electronic total energy of the optimized anionic and cationic IT-4F, respectively. These energies were evaluated using the B3LYP/6-311G(d,p) method.

Kinetic Monte Carlo simulations

The mobilities were extracted from the trajectory of charge dynamics evolved using kinetic Monte Carlo (kMC) simulations ($F = 10^5$ V/cm; simulation time 10^{-3} s). The hopping rates between any two molecules (sites) were evaluated using the Marcus theory,[48] $\omega_{ij} = \frac{J_{ij}^2}{\hbar}\sqrt{\frac{\pi}{\lambda k_B T}}\exp\left[-\frac{(\Delta E_{ij}-\lambda)^2}{4\lambda k_B T}\right]$, where T is the temperature, J_{ij} is the transfer integral between the i and j site, ΔE_{ij} is the site energy difference $E_i - E_j$, and λ is the reorganization energy. The computational details of these parameters are discussed in the subsections titled Site energy computation, Transfer integrals, and Reorganization energy.

The direct extraction of mobility from kMC simulations at 300 K suffers from the finite-size effect, which belongs to the dispersive transport regime. Therefore, we utilized the extrapolation scheme where the nondispersive mobility at 300 K could be extrapolated from the nondispersive (high-T) regime using an empirical T–μ relation.[49,50] All charge transport calculations were performed using the VOTCA package.[43]

Please note that while the EGDM, which is based on Miller–Abrahams hopping, is used to evaluate the experimental characteristics, this does not influence the experimentally obtained value of the mobility. However, there may be minor differences in the evaluated energetic disorder when comparing Miller–Abrahams hopping to Marcus hopping. In the investigated field and temperature regime, however, these differences are fairly small.[51]

RESULTS AND DISCUSSION

To characterize the electron and hole transport in IT-4F, electron- and hole-only devices were fabricated. To ensure efficient electron injection in the electron-only device, a top electrode consisting of TPBi(4 nm)/Ba(5 nm)/Al(100 nm) was used. The thin TPBi layer functions as a tunneling interlayer to form an Ohmic electron contact, which cannot be achieved with a barium layer alone, despite its low work function. The temperature-dependent electron currents are displayed in Fig. 1. The near-quadratic dependence of the current on the voltage is indicative of a space-charge-limited current that is almost trap-free. To analyze the electron currents in more detail, the J–V characteristics were fitted with a numerical

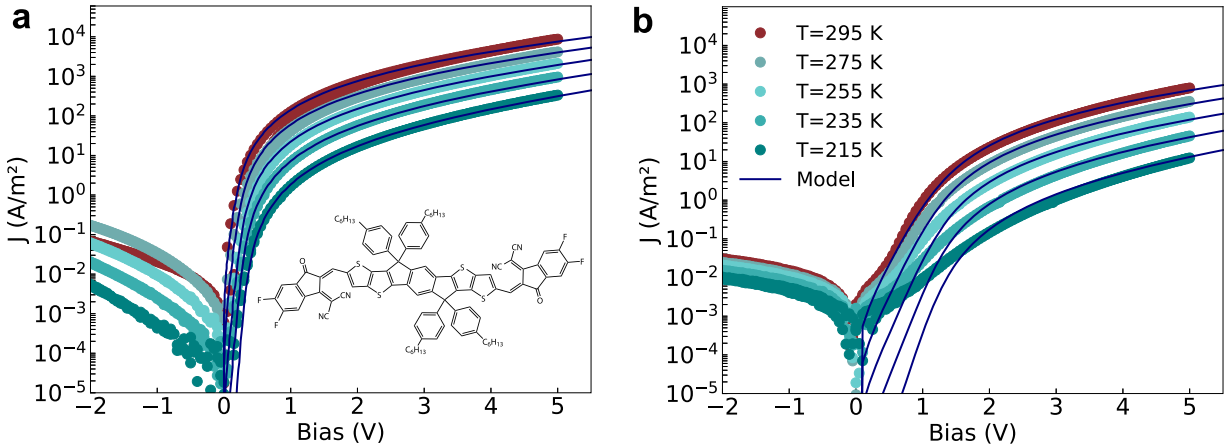

FIG. 1. Temperature-dependent *J–V* characteristics for the electron-only (a) and hole-only (b) devices comprising 200 nm pristine IT-4F films.

drift-diffusion model. In these simulations, the mobility is considered to be dependent of temperature, charge-carrier density, and electric field according to the extended Gaussian disorder model.

Electron transport

The obtained room temperature electron mobility in IT-4F is relatively high, amounting to 2.9×10^{-4} cm^2 V^{-1} s^{-1}, when extrapolated to zero electric field and zero charge-carrier density. The mobility at nonzero charge-carrier density and electric field is slightly higher, as shown in Fig. S1, which would be more representative of a solar cell under illumination. The high electron mobility is a result of the low energetic disorder of the unoccupied molecular orbitals, which can be derived from the temperature dependence of the *J–V* characteristics, where the width of the Gaussian distribution was observed to amount to 0.085 ± 0.010 eV. The narrow energetic disorder implies a significant degree of molecular ordering.

Despite the electron affinity of IT-4F (4.14 eV)[16] being situated in the trap-free window for organic semiconductors,[22] a low density of electron trap states of 8.0×10^{21} m^{-3} with a depth of 0.4 eV was identified. This low density of trap states (in the 0.01% range relative to the density of states) might originate from chemical impurities. Because the charge concentration in operating solar cells is in the 10^{22}–10^{23} m^{-3} range, these traps are easily filled and, thus, most photogenerated electrons will be free and unaffected by these traps in a solar cell (see Fig. S2 for the effect of the trap density on the *J–V* characteristics for the electron and hole transport).

When comparing the electron mobility of IT-4F to other non-fullerene acceptors, such as Y6, the mobilities seem to be quite similar. For Y6, the mobilities estimated from SCLC measurements are reported to be 1.8×10^{-4},[52] 2.15 ± 0.87 × 10^{-4},[53] and 2.35×10^{-4} cm^2 V^{-1} s^{-1}.[54]

Hole transport

To characterize the hole transport and to compare it to the electron transport, hole-only devices were fabricated and analyzed in the same manner as the electron-only devices. It was found that a MoO_3/Al hole contact could provide an Ohmic hole injection into IT-4F, having an ionization energy of 6.0 eV.[27]

The temperature-dependent *J–V* characteristics are displayed in Fig. 1(b). Despite IT-4F being known as an electron-accepting and electron-transporting material, a considerable hole current could be injected. From the fits with the drift-diffusion simulation, the hole mobility at room temperature and zero field and density was observed to be approximately one order of magnitude lower than the electron mobility, amounting to 2.0×10^{-5} cm^2 V^{-1} s^{-1}. From the temperature dependence of the hole current, the extracted energetic disorder for holes amounts to 0.110 ± 0.006 eV. This value for energetic disorder is higher than for electron transport, which is a possible reason for the somewhat lower hole mobility. The amount of hole traps is also higher than the amount of electron traps, where a concentration of 1.65×10^{22} m^{-3} was observed. This is, however, still a low concentration of traps, which is in line with the ionization energy being inside the window for a trap-free charge transport. Note that outside the trap-free window, charge-trap concentrations surpassing 10^{23} m^{-3} are typically observed, which severely hampers charge transport, as the trap density exceeds the concentration of charge carriers in organic devices.

To put the hole transport of IT-4F into perspective, the hole current in IT-4F is compared to the hole current in the donor polymer PM6 (see the supplementary material for the *J–V* characteristics). Interestingly, the observed hole currents are quite similar. The fitted hole mobility of PM6 with 5.7×10^{-5} cm^2 V^{-1} s^{-1} is only slightly higher than that of IT-4F (2.0×10^{-5} cm^2 V^{-1} s^{-1}), showing that IT-4F has decent hole transport capabilities with respect to well performing donor materials. The energetic disorder of PM6 is identified to be similar to IT-4F with 0.100 eV, as is the amount of the Gaussianly distributed hole traps in PM6 with a density of 1.5×10^{22} m^{-3}. The fact that the hole transport in IT-4F compares quite well with a state-of-the-art donor material highlights the good hole transport in IT-4F, although the hole transport in IT-4F is still inferior to the electron transport.

The mobilities found for the pristine donor and acceptor materials, although decent, appear rather low in light of the high power-conversion efficiency of 13.5% obtained for a PM6:IT-4F

blend solar cell.[25] Therefore, we assess whether there are substantial differences between the pristine-film mobilities and the mobilities obtained for a PM6:IT-4F blend. The reported mobilities for the PM6:IT-4F blend[55] (obtained by the SCLC method) are 2.11×10^{-4} and 1.95×10^{-4} $cm^2\ V^{-1}\ s^{-1}$ for electrons and holes, respectively. We obtain an electron mobility for pristine IT-4F of 2.9×10^{-4} $cm^2\ V^{-1}\ s^{-1}$, which is slightly higher than for the blend.[55] The reported hole mobility for the blend is about a factor of 3 higher than the hole mobility we obtain for PM6, which is, however, the value extrapolated to zero density and zero field. As shown in Figure S1, this amounts to a mobility in the 10^{-4} $cm^2\ V^{-1}\ s^{-1}$ range for pristine PM6 at a nonzero charge density, comparable to the value for the PM6:IT-4F blend. The minor differences between the mobility in the pristine materials are likely due to different molecular ordering in the blend. In view of the relatively low mobilities, the high power-conversion in PM6:IT-4F solar cells may rather originate from low bimolecular recombination rates, which allows for efficient charge extraction prior to recombination.

Multiscale molecular simulations

To support and further investigate the experimental observations, we simulated material morphologies using molecular dynamics simulations of 2000 IT-4F molecules and the charge transport process using kinetic Monte Carlo simulations, as described in the section titled Methods. We studied three types of molecular ordering: the crystalline, the smectic (layered), and the amorphous phase as displayed in Fig. 2. The crystalline mesophase had the highest order parameter of $S \approx 1$ and the smallest energetic disorder of $\sigma_e = 0.04$ eV. The smectic mesophase with $S \sim 0.6$ and

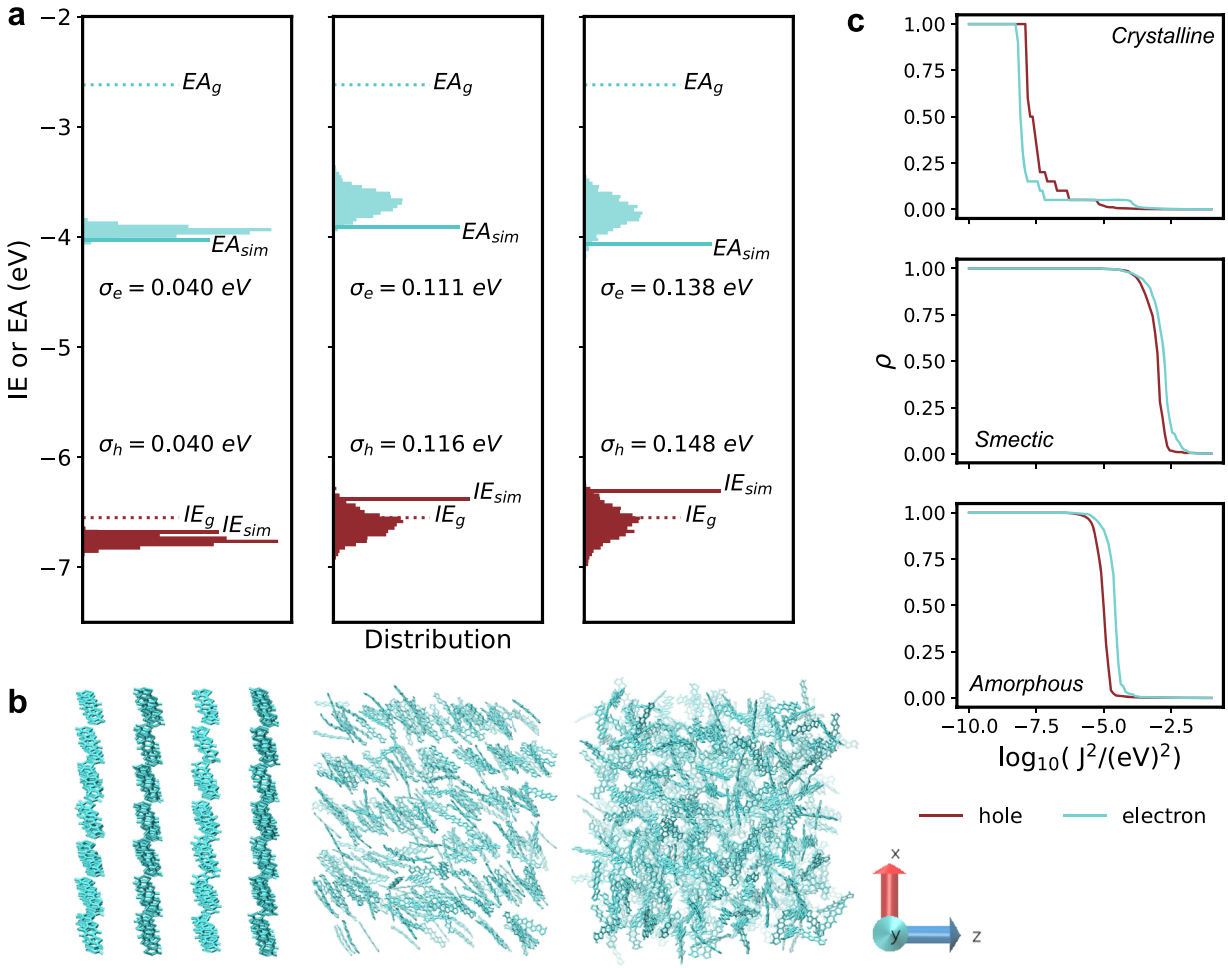

FIG. 2. (a) Energetic distribution of the density of states for the simulated phases [crystalline (left), smectic (middle), and amorphous (right)], as depicted in the snapshots (b) of a subset of the IT-4F backbones in their respective arrangement in the simulation box. The corresponding ionization energies (IE_{sim}) and electron affinities (EA_{sim}) and gas-phase energies are indicated by the solid and dashed lines in (a), respectively. (c) Percolation plot of the electron and hole transport (plot for the crystalline phase at the top, for smectic in the middle, and for amorphous at the bottom), where ρ denotes the size of the largest percolating cluster and $\log(J^2/(eV)^2)$ denotes the decadic logarithm of the dimensionless squared transfer integral J.

TABLE I. The extrapolated hole and electron mobility in *x*-, *y*-, and *z*-directions (see Fig. 2 for the orientation of the coordinate system) at $T = 300$ K and $F = 10^5$ V/cm for simulated crystalline, smectic, and amorphous morphology of IT-4F and the experimental values μ_{exp} at $T = 295$ K, extrapolated to zero electric field and zero charge-carrier density. The mobility is given in units of $cm^2\ V^{-1}\ s^{-1}$.

Hole	$\mu_{h,X}$	$\mu_{h,Y}$	$\mu_{h,Z}$	$\mu_{h,avg}$	$\mu_{h,exp}$
Crystalline	2.2×10^{-3}	8.3×10^{-2}	n.a.	4.3×10^{-2}	
Smectic	1.3×10^{-4}	2.2×10^{-4}	7.1×10^{-5}	1.4×10^{-4}	2.0×10^{-5}
Amorphous	8.2×10^{-8}	8.2×10^{-8}	8.2×10^{-8}	8.2×10^{-8}	
Electron	$\mu_{e,X}$	$\mu_{e,Y}$	$\mu_{e,Z}$	$\mu_{e,avg}$	$\mu_{e,exp}$
Crystalline	6.0×10^{-2}	4.1×10^{-1}	n.a.	2.4×10^{-1}	
Smectic	7.8×10^{-4}	3.4×10^{-4}	3.1×10^{-4}	4.8×10^{-4}	2.9×10^{-4}
Amorphous	1.6×10^{-7}	1.4×10^{-7}	1.3×10^{-7}	1.4×10^{-7}	

$\sigma_e \approx 0.12$ eV was in between the crystalline and amorphous phases, for which $S = 0.02$ and $\sigma_e \approx 0.15$ eV were calculated. The experimental value of $\sigma_e = 0.080$ eV indicates that the spin-coated IT-4F film is mostly orientationally ordered and has a partially more crystalline and partially rather smectic molecular alignment. This picture of the local morphology in IT-4F thin films is in line with a study quantifying the number of face-on interactions in dimers extracted from MD simulations[56] and can be put into context with studies on molecular packing of IT-4F.[21] Experimental 2D GIWAXS and AFM studies on IT-4F also support the existence of 10–20 nm crystalline grains in IT-4F upon annealing or treatment with an additive.[17,21,57]

For hole transport, the measured value of energetic disorder lies in between simulated $\sigma_h = 0.04$ eV (crystalline) and $\sigma_h = 0.13$ eV (smectic) mesophases. The simulated directional average hole mobility in the smectic phase of $1.4 \times 10^{-4}\ cm^2\ V^{-1}\ s^{-1}$ deviates by one order of magnitude from the experimental value of $2.0 \times 10^{-5}\ cm^2\ V^{-1}\ s^{-1}$ (Table I).

As shown in Table I, the simulated electron mobility is consistently higher (on average, $4.8 \times 10^{-4}\ cm^2\ V^{-1}\ s^{-1}$) than the hole mobility in all phases and transport directions. The small anisotropy of the mobility in the smectic phase may seem surprising: While considering the layered structure, the transport in the direction along the layers is expected to be favorable. However, two effects need to be considered here: the hopping distance is larger along the molecular axis, but the electronic coupling elements are smaller. These two effects seem to compensate each other, leading to an efficient three-dimensional ambipolar charge transport network.

Both the simulation and the experimental data provide evidence for a higher electron than hole mobility. The experimental measurements, however, yield a larger difference for both the mobility and the energetic disorder. In the multiscale simulations, the disorder values are similar for the hole and the electron transport.

Nonetheless, the higher electron mobility in all simulated phases can be explained in the framework of the hopping transport model. In this model, the low reorganization energy, high transfer integrals, and low energetic disorder are key to the high charge carrier mobility. The reorganization energies for the hole and electron of IT-4F are very similar (0.24 vs 0.25 eV), which could not explain the difference in their mobility. Instead, the transfer integral J plays a role in this case. The analysis of the size of the largest percolating cluster (Fig. 2), based on the transfer integrals between neighboring molecules, shows that in all simulated phases, the electron reaches the percolation threshold with a larger value of J as compared to the hole carrier. This result confirms the anticipated effect of the design of an acceptor–donor–acceptor molecular architecture on the favorable electron transfer. At the same time, the experimentally determined lattice constant for both types of charge transport amounts to ~2.3 ± 0.3 nm, indicating comparable hopping lengths.

CONCLUSION

The electron and hole transport in the non-fullerene acceptor IT-4F was studied by combining space-charge-limited current measurements with drift-diffusion modeling. Electron mobilities in the order of $10^{-4}\ cm^2\ V^{-1}$ were obtained, which were found to be one order of magnitude higher than hole mobilities. Low trap densities were observed for both the electron and hole transport. Values for the energetic disorder inferred from the experimental measurements amounted to 0.085 eV for electrons and 0.110 eV for holes. The ambipolar charge-transport characteristics of IT-4F were further confirmed with molecular multiscale simulations, demonstrating orientational molecular ordering and a better charge percolating network for electrons.

SUPPLEMENTARY MATERIAL

See the supplementary material for drift-diffusion simulations, experimental device characteristics, and simulated mobilities.

AUTHOR DECLARATIONS

Conflict of Interest

The authors have no conflicts to disclose.

Author Contributions

Franziska H. Hasenburg: Data curation (equal); Formal analysis (equal); Visualization (equal); Writing – original draft (equal). **Kun-Han Lin**: Data curation (equal); Formal analysis (equal); Writing – original draft (equal). **Bas van der Zee**: Formal analysis (equal). **Paul W. M. Blom**: Supervision (equal). **Denis Andrienko**: Conceptualization (equal); Supervision (equal); Writing – review & editing (equal). **Gert-Jan A. H. Wetzelaer**: Conceptualization (lead); Formal analysis (equal); Supervision (equal); Writing – original draft (equal); Writing – review & editing (equal).

DATA AVAILABILITY

The data that support the findings of this study are available from the corresponding author upon reasonable request.

REFERENCES

[1] T. Zhang *et al.*, "A medium-bandgap nonfullerene acceptor enabling organic photovoltaic cells with 30% efficiency under indoor artificial light," Adv. Mater. **34**, 2207009 (2022).

[2] M. Riede, D. Spoltore, and K. Leo, "Organic solar cells—The path to commercial success," Adv. Energy Mater. **11**, 2002653 (2021).

[3] R. Xue, J. Zhang, Y. Li, and Y. Li, "Organic solar cell materials toward commercialization," Small **14**, 1801793 (2018).

[4] M. Moser, A. Wadsworth, N. Gasparini, and I. McCulloch, "Challenges to the success of commercial organic photovoltaic products," Adv. Energy Mater. **11**, 2100056 (2021).

[5] J. Hou, O. Inganäs, R. H. Friend, and F. Gao, "Organic solar cells based on non-fullerene acceptors," Nat. Mater. **17**, 119–128 (2018).

[6] P. Cheng, G. Li, X. Zhan, and Y. Yang, "Next-generation organic photovoltaics based on non-fullerene acceptors," Nat. Photonics **12**, 131–142 (2018).

[7] A. Markina *et al.*, "Chemical design rules for non-fullerene acceptors in organic solar cells," Adv. Energy Mater. **11**, 2102363 (2021).

[8] A. Karki, A. J. Gillett, R. H. Friend, and T.-Q. Nguyen, "The path to 20% power conversion efficiencies in nonfullerene acceptor organic solar cells," Adv. Energy Mater. **11**, 2003441 (2021).

[9] J. Wang *et al.*, "A tandem organic photovoltaic cell with 19.6% efficiency enabled by light distribution control," Adv. Mater. **33**, 2102787 (2021).

[10] K. Chong *et al.*, "Realizing 19.05% efficiency polymer solar cells by progressively improving charge extraction and suppressing charge recombination," Adv. Mater. **34**, 2109516 (2022).

[11] Z. Zheng *et al.*, "Tandem organic solar cell with 20.2% efficiency," Joule **6**, 171–184 (2022).

[12] U. Würfel, D. Neher, A. Spies, and S. Albrecht, "Impact of charge transport on current–voltage characteristics and power-conversion efficiency of organic solar cells," Nat. Commun. **6**, 6951 (2015).

[13] Y. Firdaus *et al.*, "Long-range exciton diffusion in molecular non-fullerene acceptors," Nat. Commun. **11**, 5220 (2020).

[14] H. Bristow *et al.*, "Impact of nonfullerene acceptor side chain variation on transistor mobility," Adv. Electron. Mater. **5**, 1900344 (2019).

[15] N. A. Mica, S. A. J. Thomson, and I. D. W. Samuel, "Electron mobility of non-fullerene acceptors using a time of flight method," Org. Electron. **63**, 415–420 (2018).

[16] W. Zhao *et al.*, "Molecular optimization enables over 13% efficiency in organic solar cells," J. Am. Chem. Soc. **139**, 7148–7151 (2017).

[17] Y. A. Avalos Quiroz *et al.*, "Exploring charge transport in high-temperature polymorphism of ITIC derivatives in simple processed unipolar bottom contact organic field-effect transistor," Adv. Electron. Mater. **8**, 2100743 (2022).

[18] A. F. Paterson *et al.*, "N-doping improves charge transport and morphology in the organic non-fullerene acceptor O-IDTBR," J. Mater. Chem. C **9**, 4486–4495 (2021).

[19] A. Kokil, K. Yang, and J. Kumar, "Techniques for characterization of charge carrier mobility in organic semiconductors," J. Polym. Sci., Part B: Polym. Phys. **50**, 1130–1144 (2012).

[20] C. Tanase, E. J. Meijer, P. W. M. Blom, and D. M. de. Leeuw, "Unification of the hole transport in polymeric field-effect transistors and light-emitting diodes," Phys. Rev. Lett. **91**, 216601 (2003).

[21] T. J. Aldrich *et al.*, "Fluorination effects on indacenodithienothiophene acceptor packing and electronic structure, end-group redistribution, and solar cell photovoltaic response," J. Am. Chem. Soc. **141**, 3274–3287 (2019).

[22] N. B. Kotadiya, A. Mondal, P. W. M. Blom, D. Andrienko, and G.-J. A. H. Wetzelaer, "A window to trap-free charge transport in organic semiconducting thin films," Nat. Mater. **18**, 1182–1186 (2019).

[23] C. Gu *et al.*, "Recent advances in small molecular design for high performance non-fullerene organic solar cells," Mol. Syst. Des. Eng. **7**, 832–855 (2022).

[24] A. Armin *et al.*, "A history and perspective of non-fullerene electron acceptors for organic solar cells," Adv. Energy Mater. **11**, 2003570 (2021).

[25] Q. Fan *et al.*, "Synergistic effect of fluorination on both donor and acceptor materials for high performance non-fullerene polymer solar cells with 13.5% efficiency," Sci. China: Chem. **61**, 531–537 (2018).

[26] S. Karuthedath *et al.*, "Intrinsic efficiency limits in low-bandgap non-fullerene acceptor organic solar cells," Nat. Mater. **20**, 378–384 (2021).

[27] N. B. Kotadiya *et al.*, "Universal strategy for Ohmic hole injection into organic semiconductors with high ionization energies," Nat. Mater. **17**, 329–334 (2018).

[28] L. J. A. Koster, E. C. P. Smits, V. D. Mihailetchi, and P. W. M. Blom, "Device model for the operation of polymer/fullerene bulk heterojunction solar cells," Phys. Rev. B **72**, 085205 (2005).

[29] W. F. Pasveer *et al.*, "Unified description of charge-carrier mobilities in disordered semiconducting polymers," Phys. Rev. Lett. **94**, 206601 (2005).

[30] H. T. Nicolai, M. M. Mandoc, and P. W. M. Blom, "Electron traps in semiconducting polymers: Exponential vs Gaussian trap distribution," Phys. Rev. B **83**, 195204 (2011).

[31] W. L. Jorgensen and J. Tirado-Rives, "Potential energy functions for atomic-level simulations of water and organic and biomolecular systems," Proc. Natl. Acad. Sci. U. S. A. **102**, 6665–6670 (2005).

[32] W. L. Jorgensen, D. S. Maxwell, and J. Tirado-Rives, "Development and testing of the OPLS all-atom force field on conformational energetics and properties of organic liquids," J. Am. Chem. Soc. **118**, 11225–11236 (1996).

[33] A. Mondal *et al.*, "Molecular library of OLED host materials—Evaluating the multiscale simulation workflow," Chem. Phys. Rev. **2**, 031304 (2021).

[34] D. J. Cole, J. Z. Vilseck, J. Tirado-Rives, M. C. Payne, and W. L. Jorgensen, "Biomolecular force field parameterization via atoms-in-molecule electron density partitioning," J. Chem. Theory Comput. **12**, 2312–2323 (2016).

[35] T. A. Manz and N. G. Limas, "Introducing DDEC6 atomic population analysis: Part 1. Charge partitioning theory and methodology," RSC Adv. **6**, 47771–47801 (2016).

[36] A. Tkatchenko and M. Scheffler, "Accurate molecular van der Waals interactions from ground-state electron density and free-atom reference data," Phys. Rev. Lett. **102**, 073005 (2009).

[37] M. J. Frisch *et al.*, Gaussian 16 Rev C.01, Wallingford, CT, 2016.

[38] C. Poelking *et al.*, "Characterization of charge-carrier transport in semicrystalline polymers: Electronic couplings, site energies, and charge-carrier dynamics in poly(bithiophene-alt-thienothiophene) [PBTTT]," J. Phys. Chem. C **117**, 1633–1640 (2013).

[39] .L. Martínez, R. Andrade, E. G. Birgin, and J. M. Martínez, "PACKMOL: A package for building initial configurations for molecular dynamics simulations," J. Comput. Chem. **30**, 2157–2164 (2009).

[40] K. Satoh, "Relationship between thermodynamic parameter and thermodynamic scaling parameter for orientational relaxation time for flip-flop motion of nematic liquid crystals," J. Chem. Phys. **138**, 094903 (2013).

[41] M. J. Abraham *et al.*, "GROMACS: High performance molecular simulations through multi-level parallelism from laptops to supercomputers," SoftwareX **1–2**, 19–25 (2015).

[42] S. Pronk *et al.*, "GROMACS 4.5: A high-throughput and highly parallel open source molecular simulation toolkit," Bioinformatics **29**, 845–854 (2013).

[43]V. Rühle *et al.*, "Microscopic simulations of charge transport in disordered organic semiconductors," J. Chem. Theory Comput. **7**, 3335–3345 (2011).
[44]C. Poelking and D. Andrienko, "Long-range embedding of molecular ions and excitations in a polarizable molecular environment," J. Chem. Theory Comput. **12**, 4516–4523 (2016).
[45]J. Kirkpatrick, "An approximate method for calculating transfer integrals based on the ZINDO Hamiltonian," Int. J. Quantum Chem. **108**, 51–56 (2008).
[46]K.-H. Lin *et al.*, "Multiarm and substituent effects on charge transport of organic hole transport materials," Chem. Mater. **31**, 6605–6614 (2019).
[47]K.-H. Lin and C. Corminboeuf, "FB-REDA: Fragment-based decomposition analysis of the reorganization energy for organic semiconductors," Phys. Chem. Chem. Phys. **22**, 11881–11890 (2020).
[48]R. A. Marcus, "Electron transfer reactions in chemistry: Theory and experiment (Nobel Lecture)," Angew. Chem., Int. Ed. Engl. **32**, 1111–1121 (1993).
[49]A. Lukyanov and D. Andrienko, "Extracting nondispersive charge carrier mobilities of organic semiconductors from simulations of small systems," Phys. Rev. B **82**, 193202 (2010).
[50]P. Kordt, T. Speck, and D. Andrienko, "Finite-size scaling of charge carrier mobility in disordered organic semiconductors," Phys. Rev. B **94**, 014208 (2016).
[51]P. Kordt, O. Stenzel, B. Baumeier, V. Schmidt, and D. Andrienko, "Parametrization of extended Gaussian disorder models from microscopic charge transport simulations," J. Chem. Theory Comput. **10**, 2508–2513 (2014).
[52]J. Yuan *et al.*, "Single-junction organic solar cell with over 15% efficiency using fused-ring acceptor with electron-deficient core," Joule **3**, 1140–1151 (2019).
[53]G. Zhang *et al.*, "Delocalization of exciton and electron wavefunction in non-fullerene acceptor molecules enables efficient organic solar cells," Nat. Commun. **11**, 3943 (2020).
[54]W. Zhu *et al.*, "Crystallography, morphology, electronic structure, and transport in non-fullerene/non-indacenodithienothiophene polymer:Y6 solar cells," J. Am. Chem. Soc. **142**, 14532–14547 (2020).
[55]X. Du *et al.*, "Unraveling the microstructure-related device stability for polymer solar cells based on nonfullerene small-molecular acceptors," Adv. Mater. **32**, 1908305 (2020).
[56]G. Kupgan, X. K. Chen, and J. L. Brédas, "Molecular packing of non-fullerene acceptors for organic solar cells: Distinctive local morphology in Y6 vs ITIC derivatives," Mater. Today Adv. **11**, 100154 (2021).
[57]S. Marina *et al.*, "Polymorphism in non-fullerene acceptors based on indacenodithienothiophene," Adv. Funct. Mater. **31**, 2103784 (2021).